Additive Manufacturing 70 (2023) 103566

Contents lists available at ScienceDirect

Additive Manufacturing

journal homepage: www.elsevier.com/locate/addma

# 3D embedded printing of microfluidic devices using a functional silicone composite support bath

Mecit Altan Alioglu [a,b], Yogendra Pratap Singh [a,b], Momoka Nagamine [a,c], Syed Hasan Askari Rizvi [a,b], Vaibhav Pal [a,c], Ethan Michael Gerhard [a,d], Shweta Saini [a,e], Myoung Hwan Kim [a,d], Ibrahim T. Ozbolat [a,b,d,f,g,h,i,j,*]

[a] The Huck Institutes of the Life Sciences, Penn State University, University Park, PA, USA
[b] Engineering Science and Mechanics Department, Penn State University, University Park, PA, USA
[c] Department of Chemistry, Penn State University, University Park, PA, USA
[d] Department of Biomedical Engineering, Penn State University, University Park, PA, USA
[e] Department of Biological Sciences, Indian Institute of Science Education and Research Mohali, India
[f] Materials Research Institute, Penn State University, University Park, PA, USA
[g] Department of Neurosurgery, Penn State University, Hershey, PA, USA
[h] Penn State Cancer Institute, Penn State University, Hershey, PA 17033, USA
[i] Department of Medical Oncology, Cukurova University, Adana 01130, Turkey
[j] Biotechnology Research and Application Center, Cukurova University, Adana 01130, Turkey

ARTICLE INFO

*Keywords:*
Microfluidics
3D printing
Silicone composites
Embedded printing
Support bath

ABSTRACT

Over the last two decades, microfluidic devices have rapidly emerged as revolutionary platforms for research and medicine. Various kinds of materials and fabrication strategies have been used to manufacture microfluidic devices; however, most of these strategies face challenges including complexity, time consumption, and cost in recreating delicate and intricate structural organizations. Herein, a silicone composite (Si-Co) was developed and employed as a functional support bath in which a sacrificial ink was 3D printed using embedded printing, enabling freeform fabrication of complex-shaped microfluidic devices. Si-Co was a soft material that had high optical transparency and tunable mechanical properties and yield stress with self-recovering ability. Sacrificial ink filaments formed inside the Si-Co support bath were found to be stable and circular with a wide range of resolution reaching up to 50 μm in channel size. The strategy was exemplified by fabricating microfluidic devices for generation of stable microgels of various sizes. To confirm biocompatibility of Si-Co, induced-pluripotent stem cell-derived endothelial cells were lined up inside microfluidic channels to obtain vascular mimics. Additionally, proof-of-concept spheroid fabrication devices were generated. Overall, the presented strategy allows for facile, rapid, cost-effective, and high-resolution printing and presents potential for the development of microfluidic devices for various applications, such as but not limited to organ-on-a-chip devices, 3D bioprinting and drug testing.

## 1. Introduction

The field of microfluidics has grown rapidly after its introduction in the 1990 s with immense potential in developing portable, miniaturized, and low-cost devices. Initial works of Effenhauser [1] and Whitesides [2] demonstrated that low-cost microfluidic devices could be engineered using polydimethylsiloxane (PDMS) by replica molding as per a microfabricated template. Since then, PDMS has emerged as the preferred material for creating microfluidic devices for various purposes, including but not limited to organ-on-a-chip devices, tissue engineering, and point-of-care devices [3]. The wide usage of PDMS elastomer is chiefly due to its optical transparency, minimal autofluorescence, biocompatibility, moldability with submicron resolution, and high oxygen permeability [4]. Traditional methods for fabrication of microfluidic devices include photolithography, micromachining, micromilling, hot embossing, and injection molding; however, these procedures can be complex, time-consuming, expensive, difficult to modify and frequently requires the use of cleanroom facilities [5].

* Corresponding author at: The Huck Institutes of the Life Sciences, Penn State University, University Park, PA, USA.
*E-mail address:* ito1@psu.edu (I.T. Ozbolat).

https://doi.org/10.1016/j.addma.2023.103566
Received 11 January 2023; Received in revised form 18 March 2023; Accepted 17 April 2023
Available online 20 April 2023

Three-dimensional (3D) printing is a technique that has recently gained popularity for creating microdevices as it ensures precise deposition of materials to build a variety of chip designs [6]. It has emerged as a viable substitute for manufacturing of microfluidic devices with the advantages including ease of redesign and remanufacturing, no requirement for a cleanroom facility, and cost-effective setup and consumables. Currently, among the main 3D printing techniques for microfluidics include fused filament fabrication (FFF), Polyjet/MultiJet, and vat polymerization (VP) (i.e., stereolithography and digital light processing), due to their ability to generate 3D architectures and cost-effective and well-established nature with a balanced compromise between material availability and printing speed, resolution, and accuracy [7]. FFF works by heating thermoplastic filaments and extruding through a heated nozzle above their softening point with a printing resolution up to 40 μm [8]. However, shortcomings such as low precision, limited optical transparency and surface roughness limit its usage. Also, using Polyjet or Multijet, printed surface features could be enhanced, and high printing speed and accuracy can be obtained [7,9]. However, Polyjet or Multijet processes operate with a relatively high cost with chances of damaging microfluidic channels during post-processing [7,10]. On the other hand, VP possesses high printing accuracy and resolution, and generates smooth surface finish. Using VP, features below 10 μm can be achieved [11]. Its shortcomings include post treatment to remove unreacted materials, which might be cytotoxic [12], and low scalability with increasing resolution [13].

With the recent advances in 3D printing, use of PDMS for fabrication of complex structures and devices has gained substantial interest. Using PDMS, submillimeter structures and microfluidic channels with sizes ranging from 300 to 500 μm were obtained [14–16]. In our recent work, we used low-viscosity Syl184 to develop microfluidic devices, where nanoclay-reinforced Pluronic F-127 was used as a sacrificial ink to fabricate human blood vessel-on-a-chip models with relatively simple curved and straight channels [17]. However, the widely used Sylgard 184 (Syl184) is not a yield-stress material and thus not suitable for use as a support bath on its own. To produce a yield-stress material, researchers prepared a mixture by mixing two silicone-based materials: Syl184 and SE1700 [18,19]. SE1700 is a silicone elastomer paste that includes fumed silica nanoparticles. Syl184 provides the required dilution to SE 1700 to achieve the desired rheological response for 3D printing. For tunable stiffness of silicone, Durban et al. developed various custom 3D printable silicone inks with control over their chemistry, network formation, and crosslinking density. Material hardness ranging from 10 to 70 HA (Shore A Hardness) was achieved, which was suitable for various applications [20].

Towards this, embedded printing has gained considerable interest, which enables the creation of intricate architectures inside a reservoir filled with a support bath, wherein soft materials such as hydrogels can be stably printed to maintain pre-defined structures [21,22]. It involves extrusion-based printing of an ink not on a flat surface in air, but into a bath that suspends the printed ink, preventing its settling and collapsing. Thus, this strategy offers a paradigm shift in 3D printing by diminishing the need to compromise between material mimicry and manufacturability. The support bath should ideally possess yield stress and self-recovery properties to permit reversible matrix transitions from fluidized to solid-like states, thereby encapsulating, and sustaining the deposited ink [23]. Lewis et al. first demonstrated this method by writing a viscoelastic, sacrificial ink within hydrogel matrices [24]. Post printing, the matrices were cured, and the sacrificial ink was eliminated, producing a 3D network of interconnected channels. Bhattacharjee et al. printed polymer hydrogels inside a poly(acrylic acid) microparticulate Carbopol support bath and PDMS within an oil-based granular gel [25]. Hinton et al. performed embedded printing of hydrophobic PDMS prepolymer resins inside a hydrophilic Carbopol gel support. They used Syl184 to 3D print linear and helical filaments via continuous extrusion and tubular and spiral tubes via layer-by-layer fabrication, where the embedded PDMS prints were removed from the Carbopol support bath post printing and curing [26].

In this work, we developed a silicone-based composite where components including vinyl terminated polydimethylsiloxane-diphenylsiloxane (PDMS-DPS) polymer in conjunction with a hydride terminated polydimethylsiloxane-methylhydrosiloxane (PDMS-MHS) copolymer crosslinker and hydride terminated PDMS chain extender, hexamethyldisilazane (HMDS) treated silica filler, thixotropic agent, Pt catalyst, and an inhibitor 1-Ethynyl-1-cyclohexanol (ETCH) were blended using dual asymmetric centrifuge mixing system to achieve a transparent, yield-stress material, which was suitable for use as a support bath in embedded printing. Silicone composite (Si-Co) was utilized as a functional support bath to produce complex 3D structures, where the support bath was later cured and served as a microfluidic device. To exemplify the proposed strategy, microfluidic devices were fabricated to produce microgels. As a proof-of-concept, vascular mimics were generated, and spheroid fabrication devices were also 3D printed using the developed strategy. This allows the fabrication of silicone composite-based functional and biocompatible microfluidic devices in a rapid manner without the need for a cleanroom facility or complex and expensive setup.

## 2. Materials and methods

### 2.1. Materials

Vinyl terminated (4–6% diphenylsiloxane) - dimethylsiloxane copolymer 500 cSt (vPDPS) (PDV-0525), hydride terminated (25–30% methylhydrosiloxane) - dimethylsiloxane copolymer 24–60 cSt (hMDMS) (HMS-H271), hydride terminated polydimethylsiloxane 7–10 cSt (hPDMS) (DMS-H11) and Karstedt's Platinum Catalyst (SIP6831.2LC) were acquired from Gelest (Morrisville, PA, USA). HMDS treated silica (AEROSIL R 812 S) was acquired from Evonik (Essen, Germany). Thixotropic agent THI-VEX™ was obtained from Smooth-On (Macungie, PA, USA). Xanthan gum (XG) from *Xanthomonas campestris* and 1-Ethynyl-1-cyclohexanol (ETCH) were acquired from Sigma-Aldrich (St. Louis, MO, USA).

### 2.2. Xanthan gum (XG) sacrificial ink and silicone composite (Si-Co) support bath preparation

As a sacrificial ink, 3% (w/v) XG was prepared by blending XG in Dulbecco's phosphate-buffered saline (DPBS) for 4 min. After blending, XG was loaded in a 3 mL syringe, centrifuged at 4000 rpm for 5 min, and loaded onto a 3D bioprinter (Inkcredible+, Gothenburg, Cellink, Sweden) for embedded printing.

To prepare the Si-Co, 16.8 g vPDPS (84% w/w) and 0.8 g silica (4% w/w) was added to a 40 mL container and mixed at 3500 rpm for 5 min using a speed mixer DAC-330–110 SE (Flacktek Manufacturing, SC, USA). Then 0.8 g (4% w/w) thixotropic agent was added to the container and mixed at 3500 rpm for 2 min. Next, 10 μL platinum catalyst (~10 ppm) and 20 μL ETCH inhibitor (~1000 ppm) were added to the mixture and mixed at 3500 rpm for 1 min. Finally, 0.8 g (4% w/w) hPDMS and 0.8 g (4% w/w) hMDMS were added to the mixture and mixed at 3500 rpm for 1 min. This mixture was then transferred to a 10 mL syringe and centrifuged at 4000 rpm for 5 min to remove air bubbles. After centrifugation, Si-Co was loaded into a container, sacrificial ink was 3D embedded printed into it and the Si-Co was thermally crosslinked at 60 °C over 3 h. For comparison, commercial SE1700-Syl184 material was prepared by mixing the components SE1700 (Dow Corning, Auburn, MI, USA) and Syl1184 (Dow Corning) at 3500 rpm for 5 min using the speed mixer DAC-330–110 SE.

### 2.3. Rheology testing

We performed rheological measurements using an MCR 302 rheometer (Anton Paar, Austria) equipped with a 25 mm parallel plate at

room temperature (23 °C) as per the published methods [27,28]. For Si-Co samples, an amplitude sweep test was performed within a range of 0.1–200 Pa shear stress, a frequency sweep test was performed within a range of 0.1–100 rad/s angular frequency, and a thixotropic recovery sweep test was performed by applying 0.1 and 100 1/s shear rate with 60 s intervals, and a shear rate sweep test was performed within a range of 0.1–100 1/s shear rate. The catalyst was not included while preparing composites to exclude the effects of crosslinking during rheological testing.

For XG, tests were performed at 23 and 60 °C to investigate the effects of heat on the sacrificial ink properties. Storage modulus for 4% silica-0% thixotropic agent and 0% silica-4% thixotropic agent was not measured since our experimental setup was not capable of measuring the storage modulus of low viscosity Newtonian fluids accurately. Except for frequency sweep, all other tests were performed at a frequency of 1 Hz.

### 2.4. Transparency measurements

We performed transparency measurements according to our previous study.[27] Briefly, to measure the transparency of different concentrations of Si-Co and SE1700-Syl184, 100 μL of samples were first loaded into a 96-well plate and centrifuged at 2000 rpm for 5 min to remove air bubbles. Then, optical absorbances at wavelengths of 450 nm (blue), 560 nm (green) and 660 nm (red) ($n = 8$) and UV-Vis spectrum were acquired using a spectrophotometer (BioTek, Winooski, VT, USA). To demonstrate the transparency of Si-Co, samples with ~1 cm thickness were placed on a Nittany Lion Logo and printed incremental font sizes ranging from 2 to 10 points and photographed.

### 2.5. Tensile testing

Tensile mechanical tests were conducted using an Instron 5966 testing system (Instron, Norwood, MA, USA) with a 1 kN load cell and pneumatic tensile grips according to the American Society for Testing and Materials (ASTM) standard D638–14. For this, Type V dogbone samples were prepared by casting Si-Co subjected to tension at a rate of 500 mm $min^{-1}$ to failure. Values were converted to stress-strain and the initial elastic modulus was calculated from the initial gradient of the resulting curve (0–10% tensile strain).

### 2.6. Compression testing

Unconfined compression tests were performed using a 5966 series advanced electromechanical testing system with a 10 kN load cell (Instron) according to the ASTM standard D395–18. Briefly, cylindrical specimens 6 × 13 mm (height x diameter) were compressed at a rate of 1.3 mm $min^{-1}$ to failure (or to 90% strain in the case of hMDMS:hPDMS 1:7). Values were converted to stress-strain and the initial bulk modulus (kPa) was calculated from the initial gradient of the resulting curve (0–10% compressive strain).

### 2.7. Durometer testing

Cylindrical specimens of 6 × 13 mm (height x diameter) were chosen according to the ASTM standard D2240–15 for durometer testing. Tekcoplus (Hong Kong, China) shore A durometer was used to measure shore A hardness of the samples and the values were reported as Hardness A (HA).

### 2.8. Printing characterization

To characterize embedded printing of XG ink into the Si-Co support bath, Si-Co with 4% silica filler concentration was loaded into a container and 32 G (100 μm inner, 240 μm outer diameter) and 22 G (410 μm inner, 720 μm outer diameter) needles were used to investigate the effect of needle size on 3D printing. The relationship between filament diameter and printing speed was investigated by incrementally increasing the print speed from 0.25 to 2 mm/s at a 70, 105, and 140 kPa extrusion pressure for 32 G, and at a 15, 18, and 21 kPa extrusion pressure for 22 G. For circularity and roundness measurements, Si-Co with XG printed channels were crosslinked and sliced with a blade to obtain cross-sections of channels. These cross-sections were imaged with a Zeiss Axio Observer (Oberkochen, Germany) and analyzed using ImageJ (National Institutes of Health (NIH), Bethesda, MA, USA). To characterize the accuracy and printing fidelity, the XG ink was printed with a 32 G needle into Si-Co support bath with a 4% silica filler concentration. Images were taken with Zeiss Axio Observer or Zeiss Axiozoom V16 Stereo Fluorescence Microscope and analyzed using ImageJ (NIH).

### 2.9. Particle image velocimetry (PIV)

To conduct PIV tests, Si-Co with 3%, 4% and 5% silica concentrations were prepared without the catalyst. 25 μm spherical carbon particles were acquired from US Research Nanomaterials (Houston, TX, USA) and dispersed into 20% (w/v) mineral oil. 20 μL of dispersion was added to 4 g of Si-Co and mixed with the speed mixer at 3500 rpm for 5 min. We selected this mixture after preliminary efforts to have enough particles for image processing in PIV as higher particle concentration might cause opacity and carbon particle agglomeration. Inclusion of carbon particles did not change the rheological properties of Si-Co. 35 mm Petri dishes were filled with Si-Co samples and placed into a custom-made motion stage. 32 G needle was held fixed inside Si-Co while the Si-Co matrix was moved relative to the needle using the motion stage fitted with a 4 K microscope camera (HAYEAR, Shenzhen, China). Videos showing gel-needle interactions were recorded, and the motion of the tracer particles was captured at 60 fps. Images were extracted from the videos and a graphical user interface (GUI)-based open-source tool (PIVlab) in MATLAB (MathWorks, Natick, MA, USA) was used for the PIV analysis. Images were analyzed in the software using a small interrogation area occupying at least 5 tracer particles. All the images were put in pairs of two and the particles motions were linearly tracked in the frames to calculate velocity field in two-dimensional (2D) Cartesian coordinates $\left(v_x = \frac{\Delta x}{\Delta t}, v_y = \frac{\Delta y}{\Delta t}\right)$. We used a temporal field average $\left(\overline{v_x} = \frac{\sum_{i=1}^{n}(v_x)_i}{n}, \overline{v_y} = \frac{\sum_{i=1}^{n}(v_y)_i}{n}\right)$ to remove temporal noise and get an accurate estimate of the steady state velocity field and then the magnitude of the velocity field $\left(|\overline{v}| = \sqrt{(\overline{v_x})^2 + (\overline{v_y})^2}\right)$.

### 2.10. Fabrication of microfluidic devices

To fabricate microfluidic devices, Si-Co was loaded into transparent acrylic containers. Also, Petri dishes or other custom containers were used; however, some containers, like polyurethane molds, could induce surface crosslinking inhibition. To prevent this, Inhibit X (Mann Release Technologies, Macungie, PA, USA) and Ease Release 200 (Mann Release Technologies) were applied. Si-Co in containers was held under vacuum to remove air bubbles. After the removal of air bubbles, Si-Co loaded containers were placed on to the bioprinter platform. We used Inkredible+ bioprinter for 3D printing XG ink into the Si-Co support bath. G-codes were generated using MATLAB. After 3D printing, devices were kept at 60 °C in an oven over 3 h to ensure crosslinking. After crosslinking, the sacrificial ink was removed from the devices by flushing gently with water to create microfluidic channels. Since XG was water soluble, its removal was done effortlessly without damaging microfluidic channels, where water was flushed through these channels at a 100% success rate.

### 2.11. Micro-computed tomography (μCT)

To assess the topography of generated channels, μCT scanning was performed with a microCT SKYSCAN 1176 (Bruker, Billerica, MA, USA) (35 μm voxel size, 40 kV, 450 μA, and 100 ms exposure time). Image reconstruction was conducted using NRecon reconstructing software (Bruker). Rendering, smoothening, and visualization was performed using Avizo3D software (Thermo Fisher Scientific, Waltham, MA, USA).

### 2.12. Microgel production

Fish GelMA (fGelMA) was synthesized using a previously reported method [29] by reacting gelatin from cold water fish skin (Sigma-Aldrich) with methacrylic anhydride. After synthesis, fGelMA was purified using 12–14 kDa dialysis membranes and lyophilized for 2 days. For its use, fGelMA was dissolved in water to get 15% (w/v) solution and then 5% lithium phenyl (2,4,6-trimethylbenzoyl) phosphinate (LAP) (TCI chemicals, Portland, OR, USA) was added as a crosslinker. The resultant solution was used as a primary aqueous phase for microgel generation. Oil phase was prepared by mixing light mineral oil (Sigma-Aldrich) with nonionic surfactant (3% Span 80, Sigma-Aldrich) and used as a continuous phase. Different phases were injected into embedded printed microfluidic devices with controlled flow rates and rates were regulated using a syringe pump for oil flow (New Era Pump System Inc., Farmingdale, NY, USA) and a peristaltic pump (Cole Palmer, Vernon Hills, IL, USA) for fGelMA flow. Further, droplets were generated using flow focused microfluidics and generated droplets were crosslinked using 405 nm light. To get different size of microgels, three different flow rates (500, 1000, and 2000 μL/min) of continuous phase for oil and two different flow rates (1 and 30 μL/min) of aqueous phase for fGelMA were used. Microgels were imaged with an Evos XL Core microscope (Life Technologies, Carlsbad, CA, USA) and their size was quantified using ImageJ.

### 2.13. Cell culture

For biological characterization, iPSC-ECs were used. The differentiation was performed based on a previously published protocol with some modifications [30]. Human iPSC line (IMR90C4 iPSCs, WiCell Research Institute Inc, Madison, WI, USA) was cultured in mTeSR+ media on Matrigel-coated 6-well plates. Once iPSCs reached to confluency, mTeSR+ with 1 μM CHIR-99021 media was added to start the differentiation. For differentiation, the media was changed to RPMI supplemented with 50 ng $mL^{-1}$ activin A and 1X B-27 without insulin on the following day, then to RPMI supplemented with 40 ng$mL^{-1}$ BMP4, 1 μM CHIR-99021 and 1X B-27 without insulin after 15 h of incubation. After 24 h, StemPro media supplemented with $4 \times 10^{-4}$ M MTG, 2 mM L-glutamine, 50 μg $mL^{-1}$ ascorbic acid, 10 ng $mL^{-1}$ BMP-4, 5 ng $mL^{-1}$ bFGF and 300 ng $mL^{-1}$ VEGF was added and incubated for 72 h. The cells were trypisinized using Accutase and seeded with EGM-2 MV media supplemented with 20 ng $mL^{-1}$ VEGF, 20 ng $mL^{-1}$ bFGF and 1 μM CHIR-99021 on 0.1% (v/v) gelatin-coated plates. When cells reached confluency, they were trypsinized and used for experiments.

### 2.14. Cell viability and proliferation

For viability, Si-Co was cast in 24-well plates to form films and centrifuged at 2000 rpm for 3 min to remove air bubbles. After that, Si-Co was thermally crosslinked at 60 °C over 3 h and sterilized using 70% ethanol and UV treatment. The films were seeded with iPSC-ECs ($2 \times 10^6$ cells/mL). For the viability assessment, iPSC-ECs were stained using calcein AM (2 μM) and ethidium homodimer-1 (EthD-1) (4 μM). Cells were incubated with staining solutions for 30 min in an incubator and then imaged using the Zeiss Axio Observer microscope. The cellular viability was quantified by analyzing the obtained images using ImageJ. Briefly, the images were thresholded using ImageJ, the green (live cells) and red (dead cells) fluorescence intensities were quantified, and the cellular viability was reported as percent viability.

For evaluation of cell proliferation, cells were seeded on the films and assessed at Days 1 and 7. Alamar blue dye reduction assay (Invitrogen, Waltham, MA, USA) was performed as per manufacturer's protocol. Briefly, the seeded cells were incubated with 10% (v/v) of the dye for 3 h at 37 °C and read for fluorescence intensity using a microplate reader (Tecan Infinite 200 Pro, Männedorf, Switzerland) at 570/590 nm (excitation/emission). The results were presented as percent of dye reduced, which were proportional to the number of viable cells present.

### 2.15. Vascular mimic fabrication and characterization

To mimic blood vessels, devices were fabricated, each having regions of straight and a curved channel geometry. The printed devices had a single channel at a vertical angle of 30°, 60°, and 90° with respect to the horizontal line (0°). Fabricated devices were washed with 70% ethanol and DPBS multiple times to remove any remnants of the sacrificial ink followed by UV sterilization overnight. Channels were then coated with 0.1% gelatin and incubated for 2 h before seeding with cells. iPSC-ECs, at ~80% confluency, were used for perfusion experiments and seeded at a density of $30 \times 10^6$ cells $mL^{-1}$ and incubated at 37 °C for 2 h for initial cells attachment. Cell seeded devices were connected to the perfusion setup. The devices were reversed to guarantee uniform cell attachment on the upper and lower channel walls. The initial flow rate in the channel was adjusted to a value, which corresponded to a shear stress of 0.1 dyne $cm^{-2}$. After 24 h, cells in channels were fixed overnight at 4 °C using 4% paraformaldehyde (Sigma Aldrich). Then, channels were rinsed with DPBS for 30 min, permeabilized with 0.25% Triton X-100 (Sigma Aldrich) for 20 min, blocked with 1% bovine serum albumin (BSA) (Sigma Aldrich) and 10% normal goat serum (NGS) (Abcam, Cambridge, UK) in DPBS for 1 h. Then, phalloidin (Alexa Fluor 568, 1:100, Sigma-Aldrich) and Hoechst 33–258 (1:200, Sigma-Aldrich), in DPBS were introduced into the channel and incubated at room temperature for 30 min. The devices were then rinsed with DPBS for 1 h and then imaged using a Zeiss LSM 880 confocal (Oberkochen, Germany).

### 2.16. Fabrication of spheroids inside microfluidic devices

Microfluidic devices containing bifurcated channels with spherical chambers were generated. HDFs (Lonza, Walkersville, MD, USA) were cultured in Dulbecco's modified eagle medium (DMEM) supplemented (Corning, Corning, NY, USA) with 10% fetal bovine serum (R&D Systems, Minneapolis, MN, USA), 1% glutamine (Life Technologies), 1% sodium pyruvate (Life Technologies), and 1% penicillin-streptomycin (Life Technologies). HDFs were trypsinized and approximately $10^3$ cells were resuspended in 6 μL of DMEM media. The cell suspension was then seeded into each chamber of the device and incubated at 37 °C and 5% $CO_2$ for 5 h to let the cells settle down. The devices were connected to a peristatic pump (Antylia Scientific, Vernon Hills, IL, USA) to supply media at a rate of 0.5 μL/min and kept in a humidified incubator at 5% $CO_2$ and 37 °C for 2 days to form spheroids. For LIVE/DEAD assay and immunostaining, spheroids were removed from the device at Day 3 and processed. For immunostaining, spheroids were fixed in 4% paraformaldehyde, rinsed with 1X DPBS, permeabilized using 0.1% Triton-X100 for 15 min and blocked with 10% normal goat serum (NGS) and 1% bovine serum albumin (BSA) in DPBS for 1 h. Samples were incubated with Hoechst 33 258 (1:200) in DPBS for 30 min. Images were taken using a Zeiss LSM880 confocal microscope (Oberkochen, Germany). Images were analyzed using ImageJ for LIVE/DEAD assay, size and shape measurements. Additionally, spheroids were generated using HDFs cultured into each well of U-bottom 96-well plates (Greiner Bio-One, Monroe, NC) for 24 h and used for flow testing in the hourglass chambers.

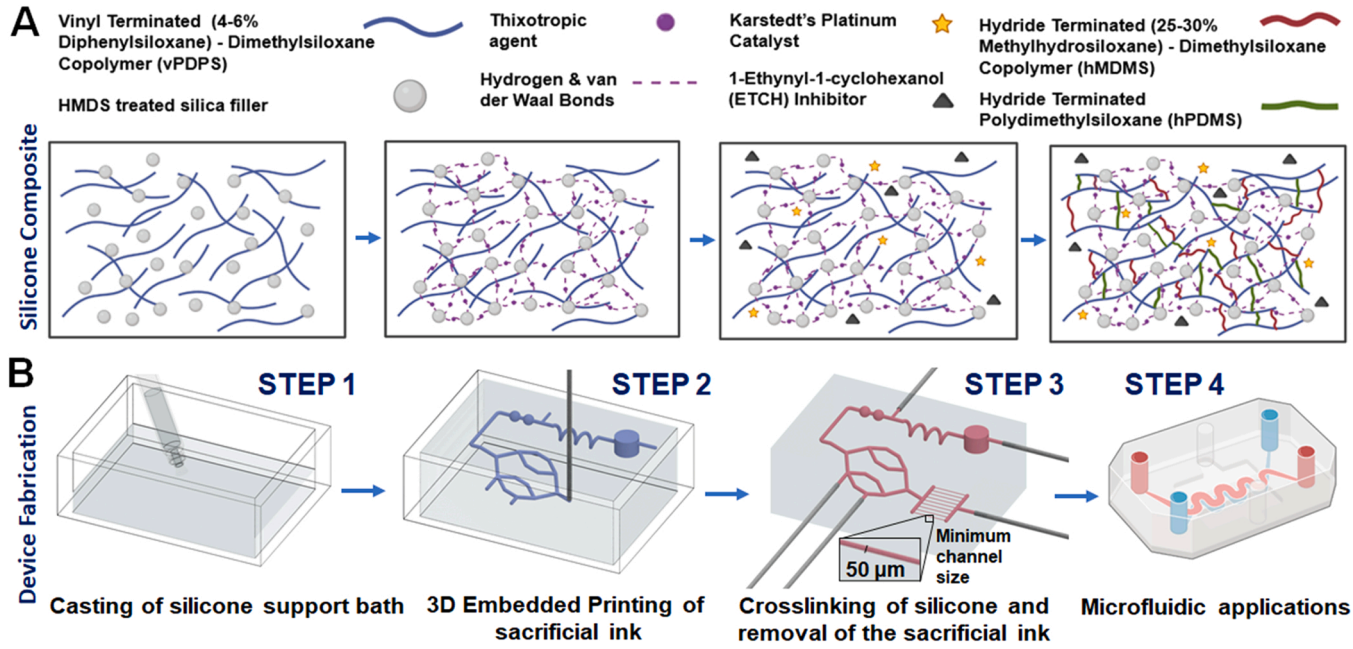


**Fig. 1.** A schematic illustrating the development of Si-Co. (A) The development of the composite silicone elastomer and (B) fabrication of microfluidic devices (created with BioRender.com).

### 2.17. Statistical analysis

All data were presented as mean ± standard deviation. Data were analyzed by OriginPro 9.1. Statistical differences were determined using one-way analysis of variance (ANOVA) with Tukey's post hoc test, and the analysis, if fulfilling the null hypothesis at $p \leq 0.05$ ( $^{*}$), $p \leq 0.01$ ( $^{**}$) and $p \leq 0.001$ ( $^{***}$) were considered statistically significant.

## 3. Results and discussion

### 3.1. Development of Si-Co material

Silicone elastomers, such as PDMS, have been widely used in microfluidics due to their elasticity, optical transparency, UV transmission, bioinertness, biocompatibility and availability [4]. Mechanical properties of silicone-based elastomers can be tuned by controlling the curing agent, conditions, and thinning reagents to suit desired applications [4]. Such characteristics have allowed research towards the development of silicone-based inks for 3D printing applications; however, most of these studies involve the use of a commercially available material, i.e., Syl184 [4]. While used as inks, silicone-based materials have not been explored as a transparent support bath for 3D embedded printing for fabrication of microfluidic devices. Towards this, we developed a composite support bath composed of vinyl terminated PDMS-DPS polymer in conjunction with a hydride terminated PDMS-MHS copolymer crosslinker and hydride terminated PDMS chain extender, along with other components including HMDS treated silica filler, thixotropic agent, Pt catalyst, and ETCH (Fig. 1**A**). To the core formulation, HMDS treated silica was added as a reinforcing filler to ensure the long-term stability of silicone components. HMDS effectively caps the silanol groups on the treated silicas, resulting in trimethylsilanes and a hydrophobic filler surface. Since hydrophobic fillers cannot create transitory networks, silicone pseudoplasticity was achieved using an extra additive. Herein, Thi-Vex, a thixotropic agent was used as an additive. Further, Platinum-catalyzed hydrosilylation chemistry was used to cure the silicone elastomer as this method produces no by-products, requires minimal amounts of catalyst or inhibitor, and can be performed under ambient temperatures [20]. Towards maximizing the working time, the ETCH inhibitor was used to slow the polymerization reaction and allow sufficient time for 3D printing inside the Si-Co support bath. The crosslinking time was tunable as per the Pt catalyst and ETCH concentrations. For example, in 20 g Si-Co material with 10 µL Pt catalyst, crosslinking at room temperature can occur within 2–3 h using 2 µL ETCH or up to 3–4 days if 20 µL ETCH is used.

For the fabrication of microfluidic devices, Si-Co was loaded into a customized container (Fig. S1) as a support bath followed by embedded printing of a sacrificial ink (Xanthan gum) within the bulk material. Subsequentially, Si-Co was crosslinked, and the sacrificial ink was removed, which enabled the generation of channels with a minimum size up to ~50 µm (Fig. 1**B**).

### 3.2. Material characterization

#### 3.2.1. Rheological assessment

To assess the suitability of Si-Co as a support bath, rheological properties were evaluated. In particular, the effect of adding a thixotropic agent and varying the amount of silica filler was investigated. Our preliminary work showed that the yield stress of 2% silica was too low, and printed filaments were displaced during deposition; while the yield stress of 6% silica was too high and made the handling and casting of Si-Co difficult. Thus, a silica filler concentration ranging from 3% to 5% was studied to gain an understanding of the role of silica concentration on rheological properties of Si-Co. Oscillatory rheology was performed and the storage ($G'$) and loss modulus ($G''$) were measured as a function of shear stress. Stress sweeps showed a linear viscoelastic (LVE) range in all samples with a dominant G' over G'', indicating a more elastic character. The cross-over point (where $G' = G''$), corresponding to the point where the material yields from solid-like to fluid-like behavior, was found to be higher at 5% followed by 4% and 3% (Fig. 2**A**). Also, the material strength increased with increasing concentration of the silica filler, which was determined by the $G'$ values in the LVE region. Further, the yield stress was determined by fitting the Herschel-Bulkley model to the data with obtained values of ~13, ~33, and ~59 Pa for 3%, 4%, and 5% silica, respectively (Fig. 2**B-C**). Increasing the amount of silica filler thus increased the yield stress of Si-Co. Viscosity curves showed the change in viscosity ($\eta$) as a function of shear rate ($\dot{\gamma}$). Viscosity of all samples decreased as the shear rate increased, demonstrating the shear thinning nature of Si-Co, with 5% silica showing the highest viscosity

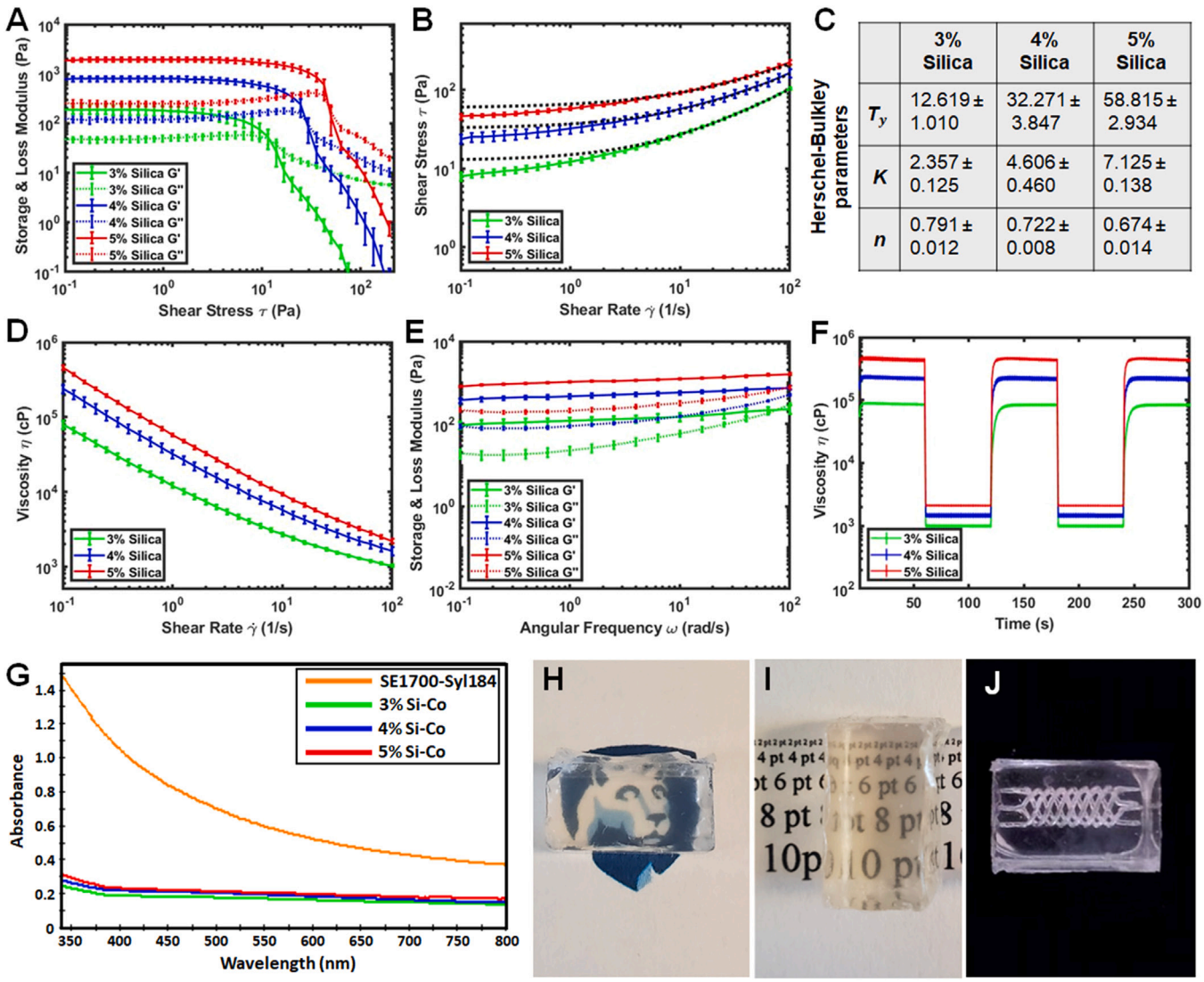


**Fig. 2.** Rheological properties and transparency of Si-Co. (A) G′ and G″ of Si-Co as a function of shear stress. (B) Shear stress as a function of shear rate where dashed lines represent Hershel-Bulkley curve fittings on the shear stress data. (C) Herschel-Bulkley parameters for the yield stress ($\tau_y$ – yield stress; $K$ – consistency index; $n$ – flow index). (D) Flow curves showing viscosity as a function of shear rate ranging from 0.1 to 100 $s^{-1}$. (E) Frequency sweep test of Si-Co in the LVE region at an angular frequency ranging from 0.1 rad to 100 rad/s. (F) Thixotropy test to assess the structural recovery of Si-Co after applying a high shear stress. The viscosity was measured at five intervals at alternating shear rates of 0.1 $s^{-1}$ for 60 s and 100 $s^{-1}$ for 60 s (G) UV-Vis spectrum of Si-Co and SE1700-Syl184 mixture. (H-I) Photographic illustrations showing the transparency of Si-Co. (J) Quadruple helix channels were visible inside a 3D printed device.

(Fig. 2**D**). Si-Co with low silica filler showed low viscosity compared to the higher silica containing Si-Co. To determine the frequency dependence of Si-Co, frequency sweep tests were carried out within the LVE region. All samples exhibited G′>G'', indicating a dominant elastic character marginally dependent on the applied frequency (Fig. 2**E**). Finally, we determined that Si-Co showed structural recovery behavior after the removal of applied higher shear rate (Fig. 2**F**).

In addition, it was observed that both silica filler and thixotropic agents were crucial to obtain a yield-stress material (Fig. S2).

### 3.2.2. *Optical Transparency*

A promising and key aspect pertinent to microfluidic devices is the transparency, which facilitates direct optical access into microchannels for accurate real-time monitoring of the process. Blended Syl184 and SE1700 have been used for embedded printing; however, the obtained material was relatively opaque making it difficult for imaging purposes [31]. After preliminary rheological and printing tests, we used the mixture of commercially available SE1700 and Syl184 (in a 60:40 ratio), which possessed yield-stress properties with potential to be used as a support bath as recently published [31] and was used as a benchmark in this work (Figs. S3A-**B**). In this regard, we printed microfluidic channels in a double helix configuration. However, opacity of the device was too high compared to the device printed using Si-Co. The transparency of the developed Si-Co was assessed via absorbance in the UV-Vis (Fig. 2**G**) and color spectrum (450 nm-blue; 560 nm-green; 660 nm-red before and after crosslinking of the material) (Figs. S3C-**E**). The absorbance value close to '0′ indicated perfect transparency without light scattering. The results showed that the optical transparency of Si-Co was significantly higher than the SE1700-Syl184 blend, as shown by the low absorbance. However, no significant difference was observed when silica concentration was varied from 3% to 5%. Interestingly, the transparency was maintained even after crosslinking of the material. Further, the transparency was demonstrated by photographic illustrations, where the Nittany Lion logo was clearly visible under Si-Co (Fig. 2**H**). The transparency of Si-Co was maintained even at a thickness of ~ 1 cm (Fig. 2**I**), where 3D complex-shaped channels inside a 3D printed device (13 ×9×7 mm) could be easily visualized (Fig. 2**J**). By incorporating pigments, absorbing, and scattering agents, the material's scattering and

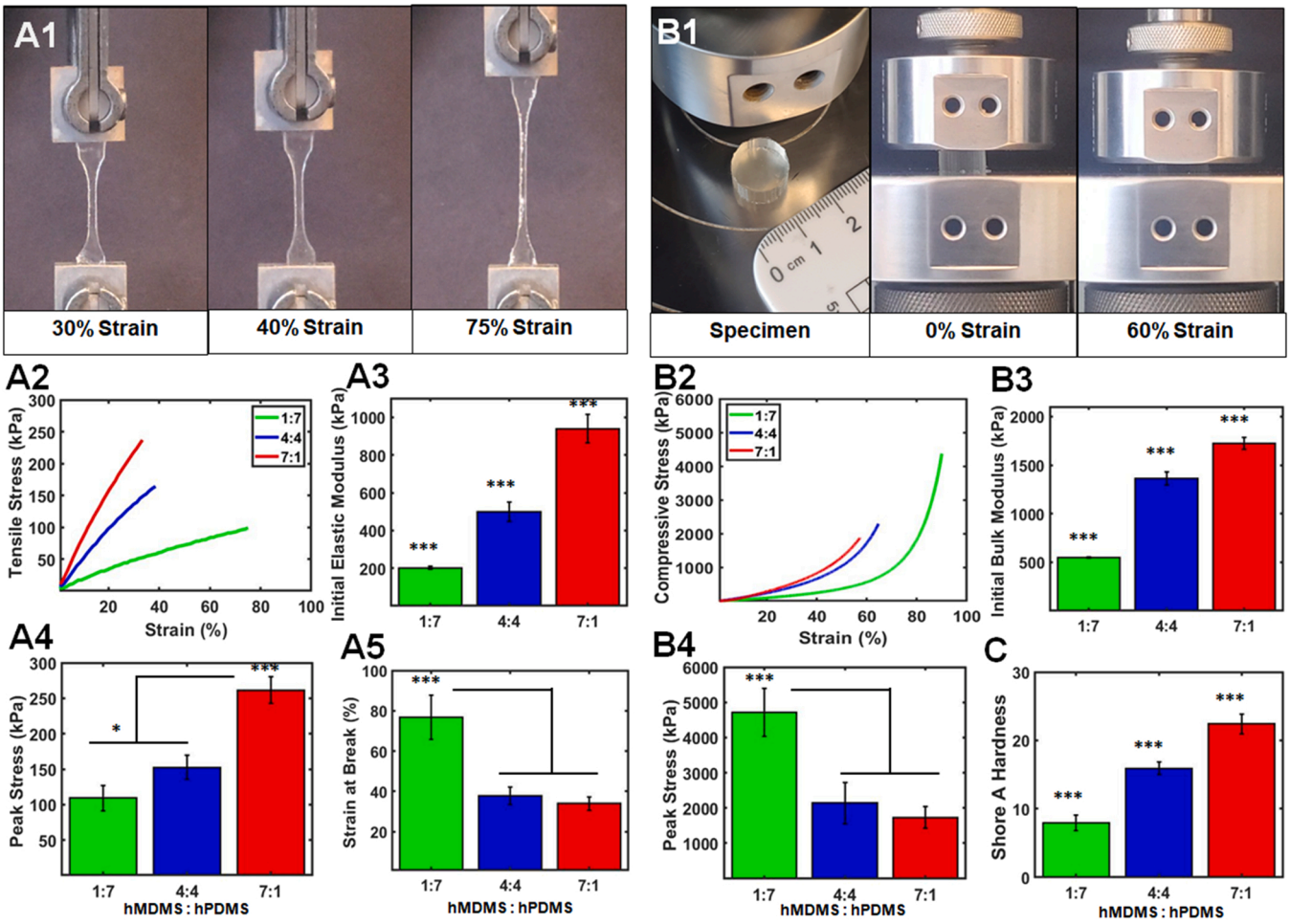


**Fig. 3.** Mechanical properties of Si-Co. (A1) Dogbone specimens were fabricated for tensile testing, (A2) tensile stress-strain curve, (A3) initial elastic modulus, (A4) tensile peak stress, and (A5) strain at break for Si-Co with varying hMDMS:hPDMS concentrations. (B1) Compressive properties of cylindrical specimens including, (B2) compressive stress-strain curve, (B3) initial bulk modulus and (B4) compressive peak stress for Si-Co with varying hMDMS:hPDMS ratios. (C) Shore A hardness of Si-Co ($n = 4$, $p^{*}<0.05$, $p^{***}<0.001$).

absorption coefficients can be further mediated to mimic the optical characteristics of various types of biological tissues due to PDMS's optical transparency and lack of a fluorescent background in the visible wavelength range [32].

### 3.2.3. *Mechanical properties*

Mechanical characterization of Si-Co was performed in tensile and compressive modes. Mechanical properties could be easily tuned by varying the hMDMS:hPDMS ratio, with higher hPDMS contents acting to increase material stiffness and tensile strength [20]. The generated Si-Co, particularly at 1:7 hMDMS:hPDMS, demonstrated considerable elasticity, with the strain at break reaching 80% (Fig. 3**A1-A2**). As stated above, a defined trend of increasing initial elastic modulus (Fig. 3**A3**) and tensile stress (Fig. 3**A4**) was observed with increased hPDMS, ranging from 200 to > 900 kPa and 100 to > 250 kPa, respectively. Concomitantly, the strain at break decreased from ~75–35% (Fig. 3**A5**). Similarly, Si-Co with higher hMDMS feeding ratios displayed significant compressive deformation prior to failure (Fig. 3**B1-B2**), with initial bulk modulus again displaying a defined increase with increasing hPDMS (from 500 to 1700 kPa, Fig. 3**B3**). However, in contrast to tensile results, peak compressive stress decreased with increasing hMDMS (from 4600 to 1700 kPa, Fig. 3**B4**), due to an observed increase in brittleness (observed as lower failure strain, Fig. 3**B2**). While 7:1 and 4:4 hMDMS:hPDMS ratios displayed fracture at 55% and 65% strain, respectively, Si-Co containing the lowest hMDMS (1:7 ratio) were not fractured even at 90% strain. Finally, Shore A hardness mirrored both tensile and compressive moduli, increasing from 8 to 22 with increasing hMDMS (Fig. 3**C**). Overall, hPDMS softened Si-Co, leading to decreased modulus, hardness, and tensile strengths; however, this enhanced flexibility contributed to decreased brittleness in compression, suggesting the importance of careful, application specific selection of the composite formulation. Mechanical properties of Si-Co were tuned by controlling the proportion of hPDMS and hMDMS amongst other factors, enabling Si-Co to mimic Young's modulus (0.1–1 MPa) of soft tissues [33].

### 3.3. *Si-Co as a support bath for embedded printing*

To fundamentally address the dilemma of choosing ink printability and biocompatibility, embedded printing is preferred as it favors accurate, continuous, and fast deposition of inks into a support bath. As opposed to granular microgels as support baths, the printing resolution of bulk material-based support baths is independent of the particle size, allowing the printing of a wide range of materials with high resolution [34]. Several materials have been used as a support bath [35]; however, silicone elastomer-based transparent support baths for embedded printing of microfluidic channels have not been demonstrated before. To test the hypothesis that Si-Co supports the formation of stable filaments, we studied the printability of Xanthan gum filaments into Si-Co.

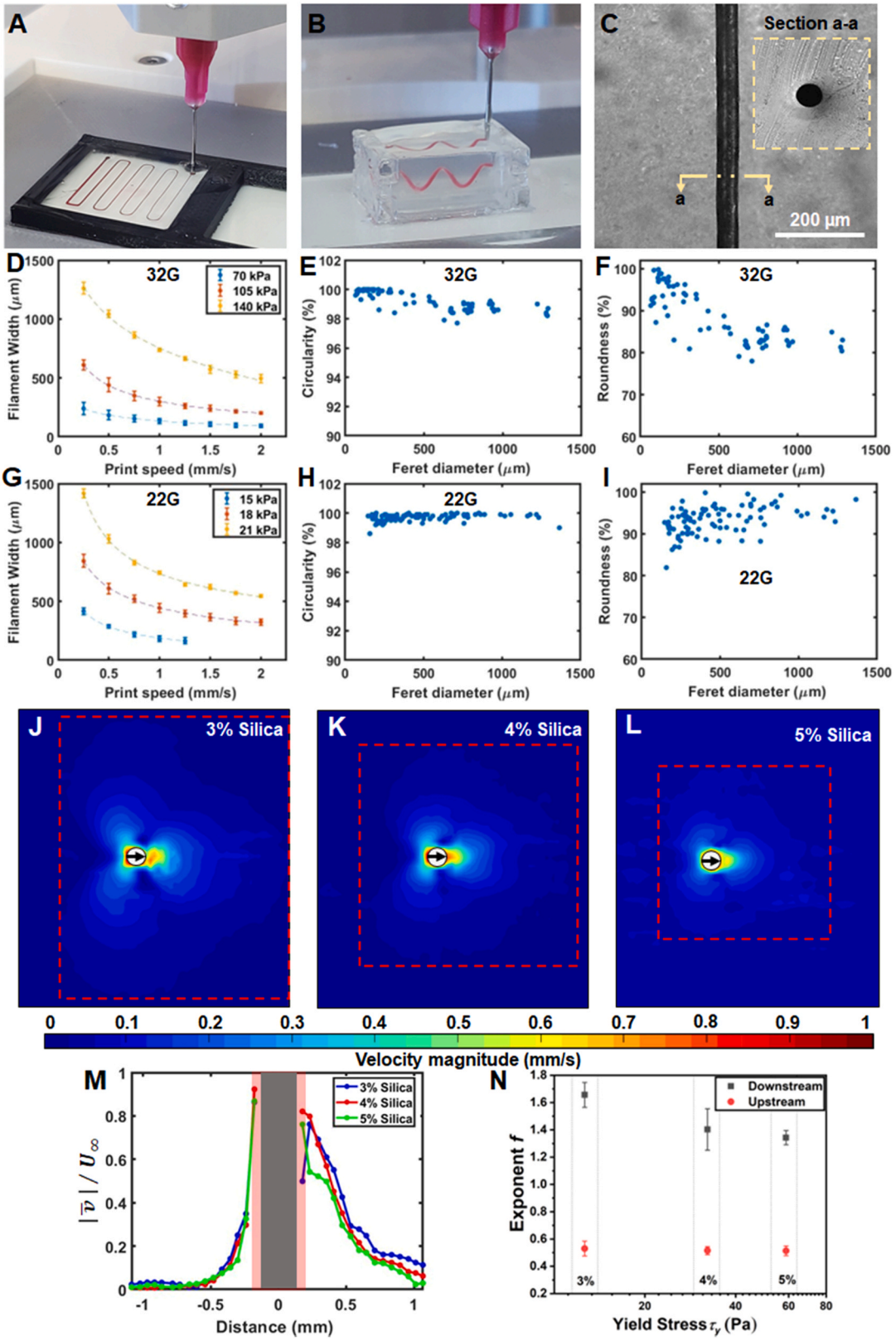


**Fig. 4.** Printing behavior of XG ink in Si-Co and PIV analysis of Si-Co. (A) Printing of a continuous filament with varying diameters, (B) 3D embedded printing of color dye-loaded spiral filament, (C) printed filament of 50 µm in diameter. (D) Filament width at different printing speeds and ferret diameter versus (E) circularity and (F) roundness using a 32 G needle. (G) Filament width at different print speed and ferret diameter versus (H) circularity and (I) roundness using a 22 G needle. Velocity flow fields of Si-Co with (J) 3%, (K) 4%, and (L) 5% silica filler around a needle moving at 1 mm/s from left to right. Red dashed box represents 3% of the printing speed. (M) Velocity decay profiles of Si-Co with different silica filler concentrations (gray area represents the needle; pink area represents the lower PIV resolution area; right side depicts the front of the nozzle (downstream); left side depicts the back of the nozzle (upstream)). (N) Exponent *f* was obtained from velocity decay profiles as a function of yield stress.

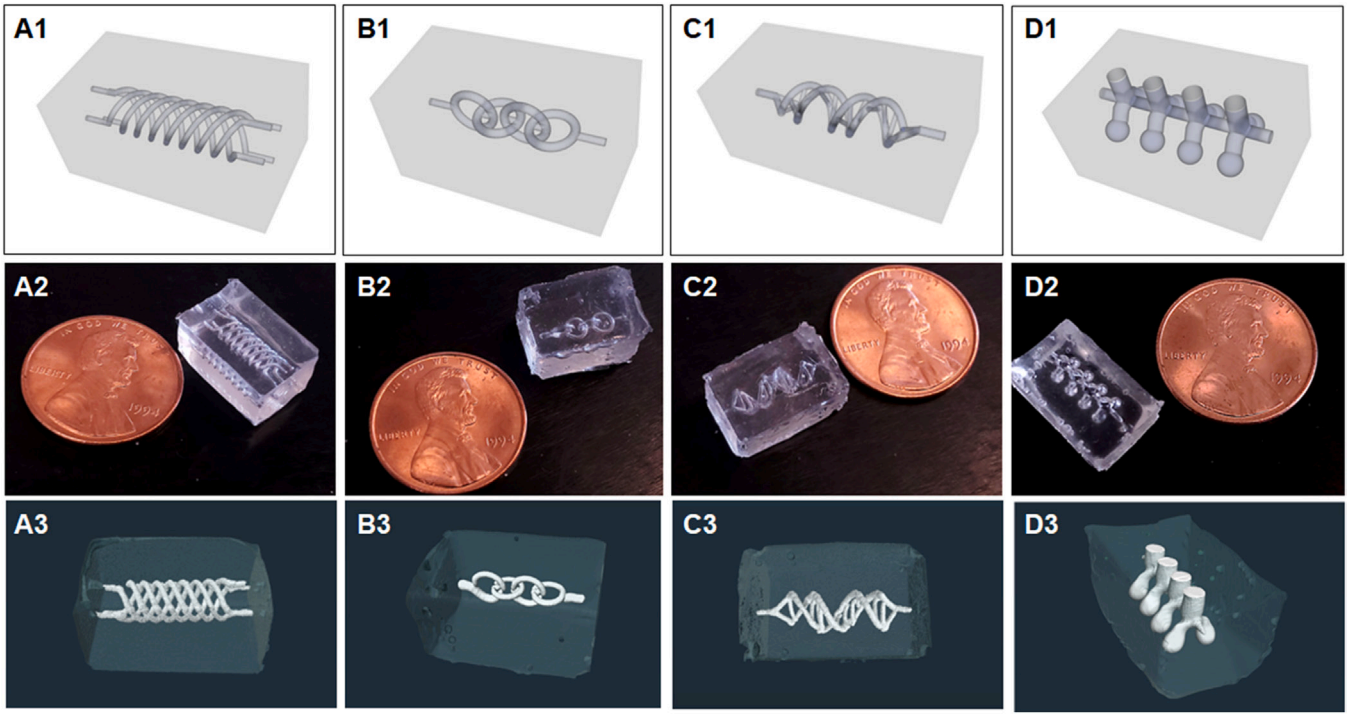


**Fig. 5.** Fabrication of complex-shaped 3D printed channels. (A) Quadruple helix, (B) linked circles, (C) a DNA model, and (D) bifurcated channels with spherical chambers. The first row represents design models, the second row shows fabricated devices, and the third row shows 3D μCT reconstruction of these devices.

*3.3.1. Printability analysis*

Here, the role of printing parameters, including printing speed, extrusion pressure, and nozzle diameter, on the width, circularity, and roundness of printed filaments were investigated. The filaments were formed using Xanthan gum (XG) ink (Fig. 4**A-B**). We used XG as our sacrificial ink due to its thermal stability [36]. Given that the fabricated devices would be thermally crosslinked at 60 ºC, we confirmed the stability of XG at this temperature as observed from the unchanged flow properties (Fig. S4). Formed filaments inside the Si-Co showed a wide range of channel sizes up to a minimum 50 μm in diameter (Fig. 4**C**). Ink extrusion was performed using 32 G and 22 G blunt straight needles. Conical needles were not selected since their outer diameter increased with distance from the nozzle tip, which would induce a larger yield region around the needle. For the 32 G needle, the results showed that the filament width increased with an increase in extrusion pressure and decreased as the printing speed was increased (Fig. 4**D**). Moreover, the formed filaments possessed a circularity of ~98% while the roundness ranged from 80% to 98% (Fig. 4**E-F**, S5). It was observed that with increasing extrusion pressure, slightly ellipsoidal-shaped filaments were formed. This may be due to the increasing difference between filament and nozzle diameter. Similarly, for the 22 G needle, the filament width increased with an increase in extrusion pressure and decreased as the printing speed increased (Fig. 4**G**). However, at printing speeds higher than 1.25 mm/s, printed filaments broke. Formed filaments showed a circularity of ~99% while the roundness ranged from 82% to 98% (Fig. 4**H-I**). Since the utilized needles were circular, circular or elliptical channels were obtained; however, needles with different geometries can be used to fabricate different shape channels [37].

To test the accuracy of printed samples, filaments with gaps of 1–3 mm were printed and the distance between filaments were measured after printing (Fig S6 **A1–4**). One of the limitations of embedded printing is the effect of printing path on print fidelity [31]. While the needle crosses an existing filament, it can easily move the filament. This effect makes printing of intersected filaments challenging. To investigate this, bi-layered grid structures with varying pore sizes were printed and the printability analysis was performed according to the literature [17]. The bi-layer grid with 500 μm distance showed decent printability (Fig S6 **B1–4**); however, the bi-layer grid with no distance showed poor printability since layers overlapped each other on their edges and intersections caused filaments to displace (Fig S6 **C1–4**). To overcome this challenge, further research can be conducted on the optimization of printing parameters (Fig S6 **D1–4**), printing path, support bath and sacrificial ink selection.

*3.3.2. Particle image velocimetry (PIV)*

To investigate how the field around the needle changes as the needle moves (Video 1) and to observe the effects of changing silica concentration on such a field, we conducted PIV experiments by adding carbon microparticles and recording the field around the needle with a microscopic camera (Figs. S7A-**B**). Inclusion of carbon particles did not change the rheological properties of Si-Co (Figs. S7C-**D**). Fig. 4**J-L** show a plot of velocity ($\bar{v}$) field for 3%, 4%, and 5% silica Si-Co, respectively, at a printing speed of $U_\infty = 1\text{mm/s}$. A red box was used to envelop the 3% level-set of the printing speed. The size of the envelope decreased as the percentage of silica filler increased. The envelope qualitatively represented the spatial disturbance and therefore the yield region of Si-Co. We found that Si-Co behaved like a viscoelastic solid below the yield stress and a Herschel-Bulkley fluid beyond the yield stress. Hershel-Buckley model did not incorporate thixotropy dealing with time-dependent breaking and buildup of Si-Co after shearing around the nozzle. To better understand this breakup and buildup behavior, we plotted the velocity profile for each gel downstream (right, in front of the nozzle) and upstream (left, behind the nozzle) in Fig. 4**M** and an exponential decay model for the velocity [31,38,39] was fitted to the data:

$$\frac{|\bar{v}|}{U_\infty} = e^{-\frac{r}{f a}} \tag{1}$$

where $r$ is the distance from the nozzle and $f$ is a characteristic parameter for the velocity decay. The large difference between the upstream and downstream velocity decay "$f$" parameter showed that Si-Co was highly thixotropic in nature. As the yield stress of Si-Co increased, a faster exponential decay was observed (Fig. 4N). The observed velocity field

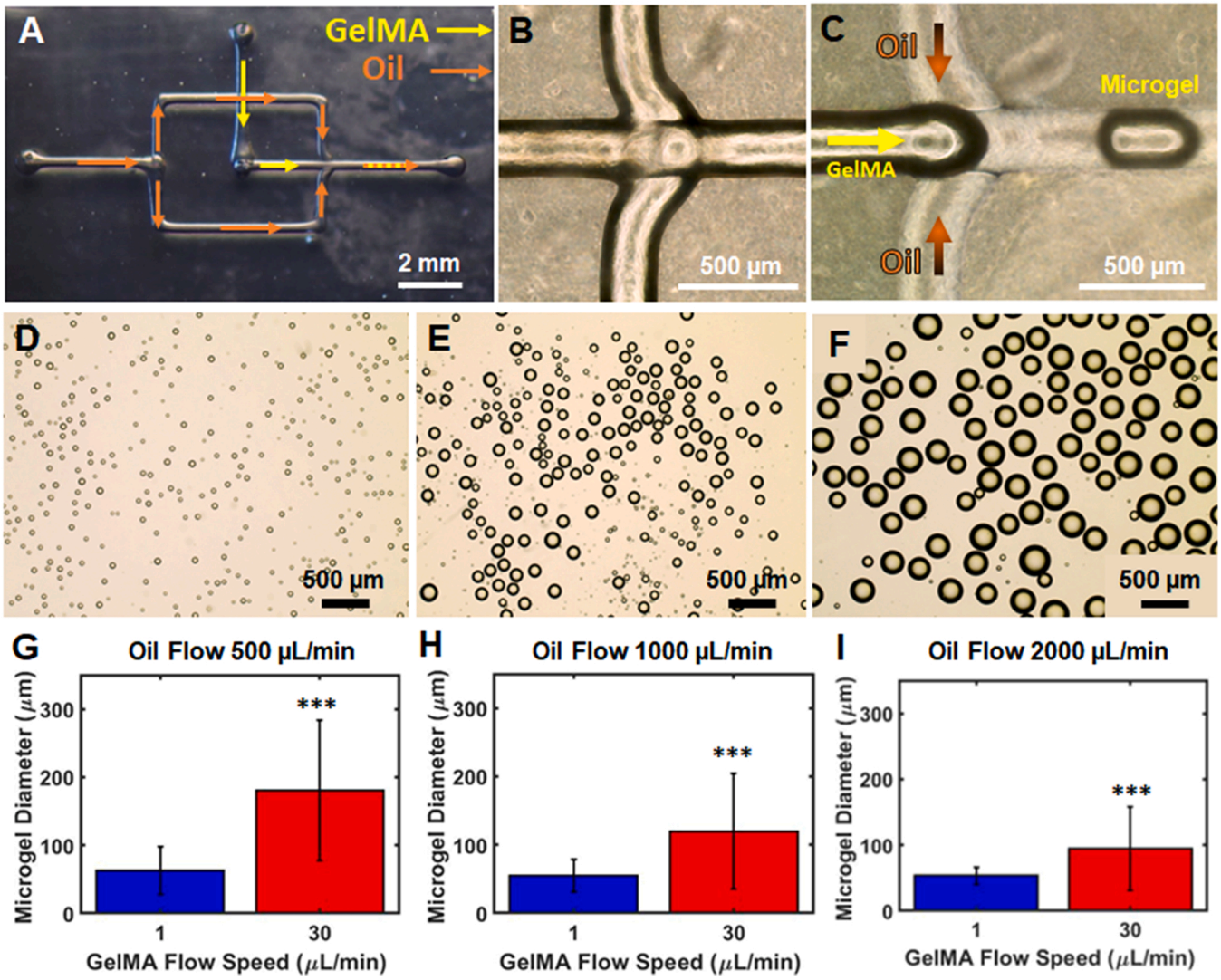


**Fig. 6.** Fabrication of a microfluidic device for microgel production. (A) A fabricated microfluidic device with GelMA prepolymer as a dispersed phase in a continuous oil phase, (B) the junction of the device, and (C) formation of single microgel. (D-F) Morphology of the produced microgels at varied sizes, and (G-I) microgel diameter with varying GelMA and oil flow rates ($n > 105$, $p^{***}<0.001$).

pattern was not symmetric upstream and downstream, which could be expected for non-thixotropic Herschel-Bulkley fluids as shown in numerical *in-silico* experiments [40].

### *3.4. Exemplification of embedded printing in Si-Co for fabrication of 3D devices*

#### *3.4.1. 3D printing of microfluidic devices*

Using embedded printing, we demonstrated complex-shaped 3D channels in Si-Co support bath enabled devices. As shown in Fig. 5**A1-D1**, we fabricated quadruple helix, linked circles, a DNA model, and a bifurcated tube with spherical chambers. These were self-standing hollow devices (Fig. 5**A2-D2**). It is pertinent to note that the channels were interconnected with either a single or multiple inlets and outlets as shown in µCT images (Fig. 5**A3-D3**). To demonstrate the connectivity and flow ability of these channels, we perfused various dye-based solutions through the intertwined channels of the quadruple helix (Video 2). By increasing the level of complexity, we also fabricated hourglass and showed the flow of spheroids from one chamber to another (Video 3).

#### *3.4.2. 3D printing of a microfluidic device for microgel production*

To demonstrate the utility of the presented approach, a facile hydrodynamic flow focusing device was 3D printed and used for microgel production. The device made of Si-Co had a channel diameter of ~250 µm. Microgels were generated using a dispersed phase of GelMA prepolymer in a continuous oil phase on the flow-focusing microfluidic junction of the platform (Fig. 6**A-C**, Video 4). Flow rates of 1 and 30 µL/min for GelMA prepolymer and 500, 1000, and 2000 µL/min for mineral oil were tested. Microgels with sizes ranging from 20 to 300 µm were obtained based on varying flow rates (Fig. 6**D-F**). The results indicated that at a constant oil flow, the microgel diameter increased significantly with an increase in GelMA flow rate (Fig. 6**G-I**). At the lower GelMA flow rate (1 µL/min), there was no significant difference in microgel size even with an increase in oil flow rate. However, at the higher GelMA flow rate (30 µL/min), the microgel size decreased with increasing oil flow rate. Smaller as well as larger microgels were generated at a higher GelMA flow rate of 30 µL/min, causing a high variation in microgel size. Therefore, further optimizations can be employed to deploy the presented device for fabrication of microgels for applications with different microgel size requirement.

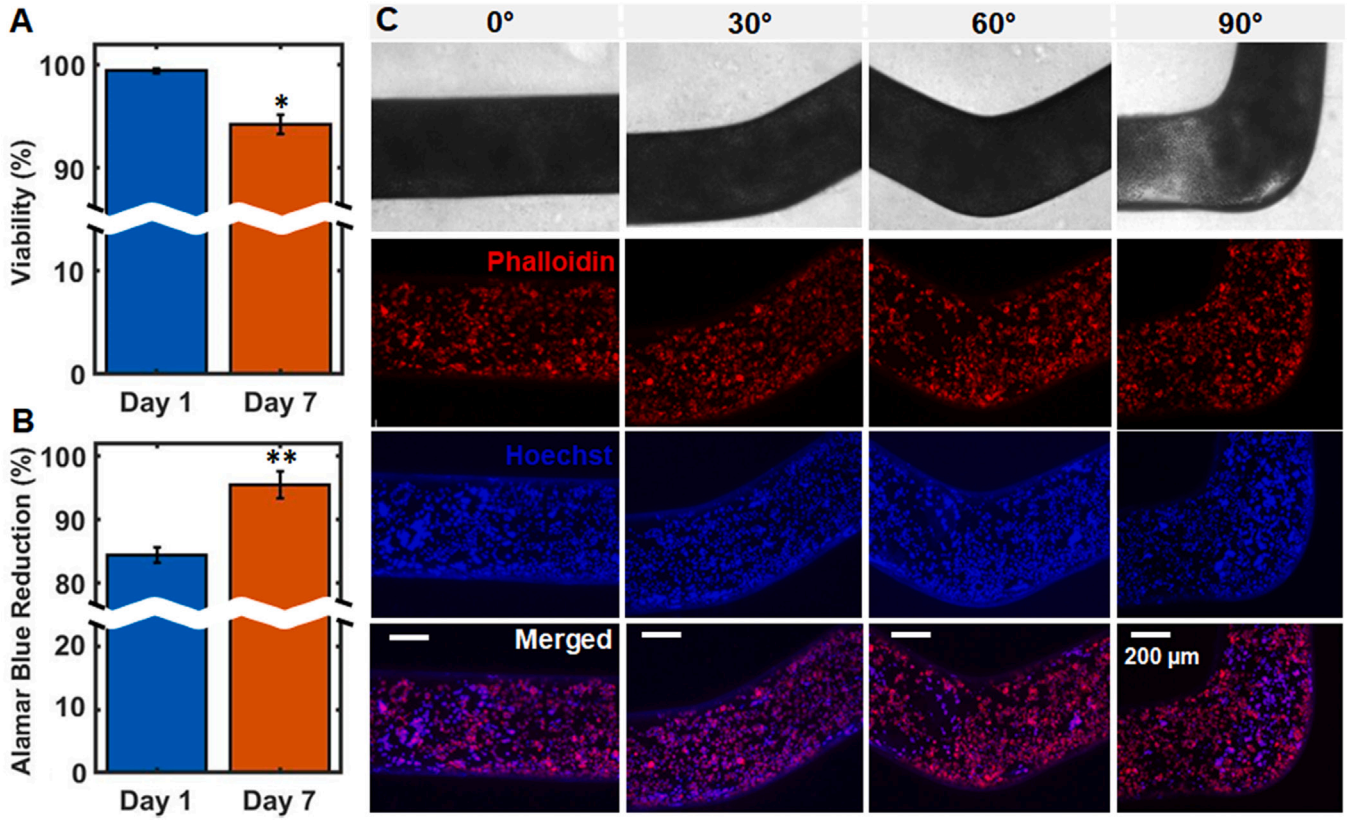


**Fig. 7.** Viability and proliferation of iPSC-ECs on Si-Co and microfluidic channels seeded with iPSC-ECs. (A) LIVE/DEAD assay showing the viability of iPSC-ECs, and (B) Alamar blue reduction assay showing proliferation of iPSC-ECs on 0.1% gelatin-coated Si-Co after Day 1 and 7 ($n = 5$, $p^{**} < 0.01$). (C) iPSC-ECs were stained with phalloidin (red) to visualize their actin cytoskeleton and nuclei stained with Hoechst (blue). Confocal images of devices having channels with no curvature (0°) and curvatures of 30°, 60°, and 90° were evaluated.

### *3.5. 3D printing of a vascular mimic*

Reproducible systems that closely mimic vasculatures are required to comprehend how blood arteries form and function. A strategy based on microfluidic vessels offers a potential step toward this objective. In terms of biological applications, PDMS plays a significant role as a structural material for in vitro and in vivo studies [41]. Cells, including endothelial cells, can be grown on PDMS to improve its function as the mechanical support of blood vessel models, making them more suitable for cell-based microfluidics investigations [42].

In this study, towards a promising cell source, we used induced pluripotent stem cell (iPSC) derived endothelial cells (iPSC-ECs) to assess the biocompatibility of the developed Si-Co material. In this regard, iPSCs were first differentiated to ECs and then seeded onto Si-Co coated with 0.1% gelatin. After initial cell attachment, samples were cultured further for 7 days. Cells exhibited adhesion and homogenous distribution on Si-Co coated with 0.1% gelatin (Figs. S8A-**B**). For the viability assessment, iPSC-ECs were stained using Calcein-AM (live cells stained green) and EthD-1 (dead cells stained red). ~95% cell viability was maintained at Day 7 (Fig. 7**A,** Fig. S9). Further, Alamar blue reduction results showed a statistically significant increase in the metabolic activity of cells, indicating their higher proliferation at Day 7 compared to that at Day 1 ($p \leq 0.01$) (Fig. 7**B**). These results demonstrate the biocompatibility of Si-Co and its suitability for potential biological applications.

Although conventional strategies, such as soft lithography, have been commonly used to fabricate vascular mimics using microfluidic channels in PDMS-based devices, the geometries of these channels are usually straight with square or rectangular cross-sections due to fabrication limitations, which may not fully capture the complex curvatures and irregularities found in native blood vessels [43,44]. Indeed, Pollet et al. simulated the flow behavior in circular versus square cross-sectional channels of similar dimensions and reported that it is essential to have circular rather than square or rectangular cross-sections to mimic blood vessels [45]. In this regard, several studies have demonstrated embedded bioprinting of complex-shaped vascular networks with a circular cross-section [46,47]; however, generation of such in PDMS-based devices have yet to be demonstrated. Towards this, we fabricated straight as well as curved circular channels, mimicking native blood vessel alignment using the ability of embedded printing. In this regards, three different curvatures were incorporated including 30°, 60°, and 90° with a diameter of 500 µm. iPSC-ECs were seeded inside 0.1% gelatin coated channels and cultured for 24 h. Results revealed that phalloidin and Hoechst-stained cells exhibited homogenous distribution throughout the channels after 24 h of perfusion (Fig. 6**C**). The results were in agreement with a previous report where HUVEC-seeded on fibronectin-coated curved PDMS channels showed good attachment and distribution towards a blood-vessel-on-a-chip model [17].

Moreover, as a proof-of-concept, microfluidic devices were developed for fabrication of spheroids (Fig. 8**A-B**). Human dermal fibroblasts (HDFs) were seeded inside microfluidic devices having bifurcated channels with spherical chambers (Fig. 5 D1–3). Similar to conventionally fabricated spheroids in cell-repellant 96-well plates, HDFs aggregated and formed spheroids by Day 2 under perfusion (Fig. 8**C-D**). In 3D printed proof-of-concept devices, only 8 spheroids were generated per device; however, these devices can be scaled up to achieve high-throughput fabrication of spheroids. Furthermore, different types of cells were used to form heterocellular spheroids. More specifically, HDFs and MDA-MB-231 cells were cocultured in 4:1 ratio for two days yielding stable spheroids (Fig. 8**E**). To compare spheroids generated in

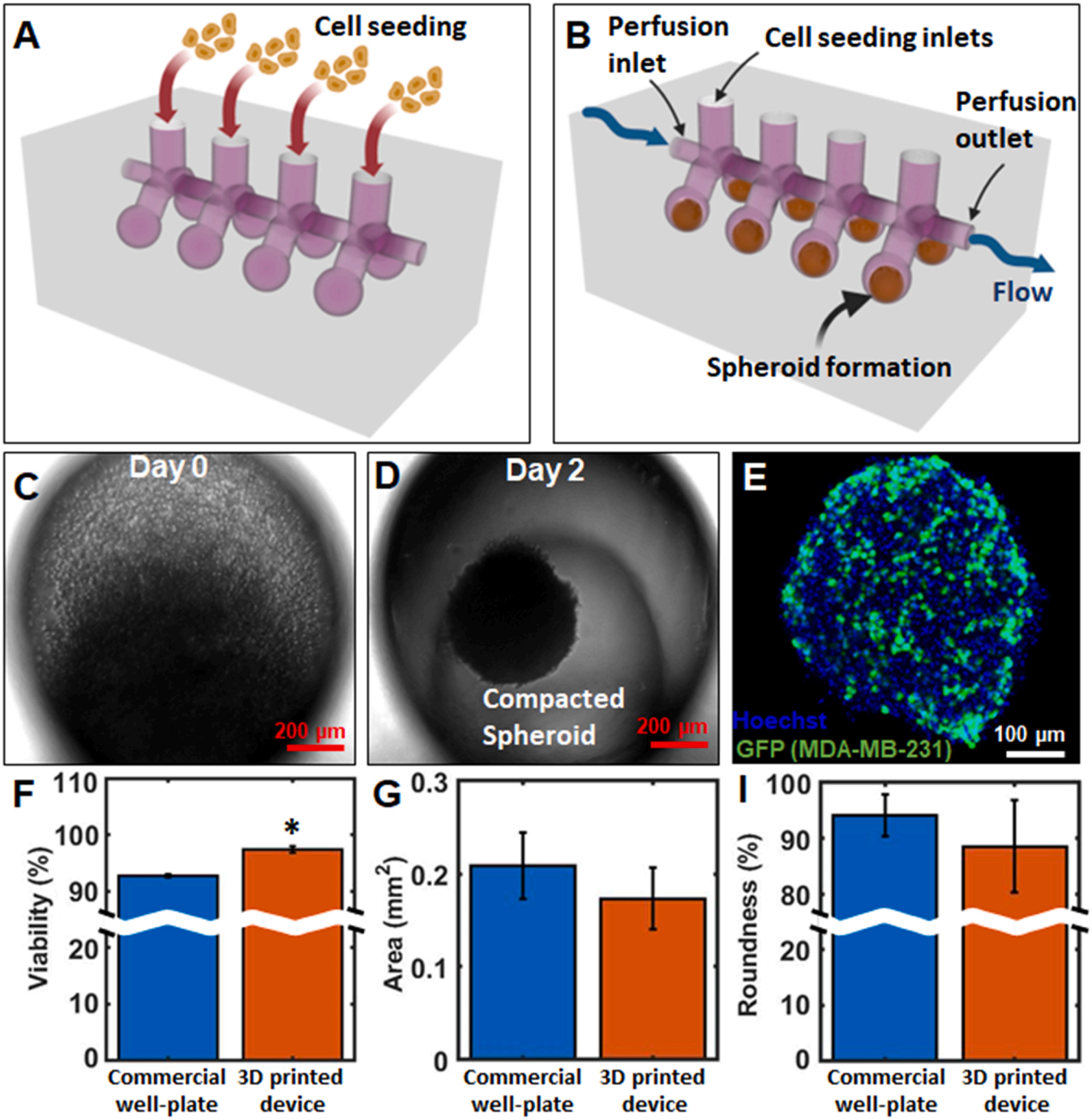


**Fig. 8.** Microfluidic devices for fabrication of spheroids. Schematics of demonstrating (A) cell seeding into microfluidic devices and (B) spheroid formation inside these devices. (C) HDFs inside the chambers after seeding. (D) Spheroid formation on Day 2. (E) A Hoechst stained HDF and $GFP^{+}$ MDA-MB-231 heterocellular spheroids. (F) LIVE/DEAD assay showing the viability, ($n = 3$, $p^{*}<0.05$). (G) surface area and (I) roundness of spheroids generated in 96-well plates and 3D printed microfluidic devices ($n = 5$).

devices with spheroids generated in commercial well plates, LIVE/DEAD (Fig. 8**F,** Fig. S10), size and shape analysis (Fig. 8**G-I**) were conducted. Spheroids generated in printed devices had higher viability and similar size and shape compared to spheroids generated in commercial 96-well plates. Higher viability could be due to fact that active perfusion was applied in microfluidic devices while static culture conditions were maintained in 96-well plates These perfusable devices can be used for developing drug testing platforms for cancer therapeutics, spheroid-on-a-chip applications or spheroids can be removed from the devices for further applications including aspiration-assisted bioprinting [48].

In this work, a novel silicone composite with high optical transparency, tunable yield stress with a structural-recovery ability was developed. This allowed the fabrication of Si-Co-based functional and biocompatible microfluidic devices in a rapid manner without the need for a cleanroom facility or complex and expensive setup. The presented technique is versatile with the ability to form stable channels with sizes ranging from 50 μm to > 1 mm in a single print. As shown in Table S1, compared to the existing 3D printing techniques utilized for fabrication of microfluidic devices [49], the presented technique was faster and relatively straightforward that can be performed using an inexpensive

setup. Extrusion printers, those custom made [50] or available commercially, can be utilized.

Although the current strategy has several advantages including ease of fabrication, rapid production of devices and cost-effectiveness, there are some limitations, which need to be addressed in future studies. For example, the minimum channel size that could be achieved was 50 μm. To advance this, printing conditions can be further optimized, and new materials can be developed. Also, $< 150$ μm channels can be printed following straight paths only as paths with corners or branched network were a challenge. Additionally, the support bath took over 2 h to crosslink, which could be shortened using light-induced crosslinking. Another downside was the step involving the degassing process, which is typically cumbersome using silicone-based materials. Embedded printing with cell-laden bioinks into silicone can also be considered in the future; however, the current method utilized heat and required over 2 h to crosslink. Thus, it might not be suitable for cell deposition. The use of other crosslinking techniques including photocrosslinking may help overcome this challenge.

## 4. Conclusion

Embedded printing is an emerging technique for fabrication of soft material-based tissues and devices; however, embedded printing using silicone-based materials as functional support baths remains unexplored. Towards this, we reported the development of a silicone composite that is optically transparent with appealing yield-stress and self-recovering properties favoring its use as a support bath for embedded printing. By modulating material composition, rheological and mechanical properties, and crosslinking times can be tuned for desired applications. Using the developed Si-Co support bath, a thermally-stable sacrificial ink was utilized to fabricate complex-shaped microfluidic channels in a rapid and cost-effective manner without any need for cleanroom facilities. To exemplify the approach, we fabricated flow-focusing microfluidic devices for generation of microgels. The developed material was found to be biocompatible with iPSC-ECs demonstrating their adhesion and proliferation. Additionally, we showed the capability of this strategy to facilitate the formation of vascular mimics and enable fabrication of a 3D microfluidic device for spheroid generation. Overall, the reported strategy involving silicone composite for embedded printing to fabricate microfluidic channels with higher complexities at greater resolutions, has immense potential for a wide range of applications including but not limited to organ-on-a-chip platforms and other biodevices.

## CRediT authorship contribution statement

**Mecit Altan Alioglu**: Writing – original draft, Visualization, Validation, Methodology, Investigation, Conceptualization. **Yogendra Pratap Singh**: Writing – review & editing, Writing – original draft, Investigation. **Momoka Nagamine**: Writing – original draft, Investigation. **Syed Hasan Rizvi**: Investigation. **Vaibhav Pal:** Investigation. **Ethan Michael Gerhard**: Investigation. **Shweta Saini**: Investigation. **Myoung Hwan Kim**: Investigation. **Ibrahim Ozbolat:** Writing – review & editing, Supervision, Funding acquisition, Conceptualization.

## Declaration of Competing Interest

I.T.O. has an equity stake in Biolife4D and is a member of the scientific advisory board for Biolife4D, Healshape and Brinter. Other authors declare that they have no known competing financial interests or personal relationships that could have appeared to influence the work reported in this paper.

## Data Availability

Data will be made available on request.

## Acknowledgments

This research has been funded by the Humanitarian Materials Program at the Materials Research Institute at Penn State, National Science Foundation Award 1914885, and 2236 CoCirculation2 of TUBITAK Award 121C359. The authors would like to thank Dr. Deepak Gupta (Penn State) for MicroCT imaging, Dr. Thomas Neuberger (Penn State) for microCT facilities and the Penn State Media & Technology Support Services for providing high-resolution cameras for imaging purposes. The authors are also grateful to Dr. Jiang Yang (Penn State) for providing mechanical testing facilities and Dr. Francesco Costanzo for providing help with PIV analysis.

## Appendix A. Supporting information

Supplementary data associated with this article can be found in the online version at doi:10.1016/j.addma.2023.103566.

## References

[1] C.S. Effenhauser, G.J.M. Bruin, A. Paulus, M. Ehrat, Integrated capillary electrophoresis on flexible silicone microdevices: analysis of DNA restriction fragments and detection of single DNA molecules on microchips, Anal. Chem. 69 (1997), https://doi.org/10.1021/ac9703919.
[2] Y. Xia, G.M. Whitesides, Soft lithography, Annu. Rev. Mater. Sci. 28 (1998), https://doi.org/10.1146/annurev.matsci.28.1.153.
[3] J.B. Nielsen, R.L. Hanson, H.M. Almughamsi, C. Pang, T.R. Fish, A.T. Woolley, Microfluidics: innovations in materials and their fabrication and functionalization, Anal. Chem. 92 (2020), https://doi.org/10.1021/acs.analchem.9b04986.
[4] I. Miranda, A. Souza, P. Sousa, J. Ribeiro, E.M.S. Castanheira, R. Lima, G. Minas, Properties and applications of PDMS for biomedical engineering: a review, J. Funct. Biomater. 13 (2022), https://doi.org/10.3390/jfb13010002.
[5] S.M. Scott, Z. Ali, Fabrication methods for microfluidic devices: an overview, Micro (Basel) 12 (2021), https://doi.org/10.3390/mi12030319.
[6] A. v Nielsen, M.J. Beauchamp, G.P. Nordin, A.T. Woolley, 3D printed microfluidics, Annu. Rev. Anal. Chem. 13 (2020), https://doi.org/10.1146/annurev-anchem-091619-102649.
[7] G. Gonzalez, I. Roppolo, C.F. Pirri, A. Chiappone, Current and emerging trends in polymeric 3D printed microfluidic devices, Addit. Manuf. 55 (2022), 102867, https://doi.org/10.1016/j.addma.2022.102867.
[8] M.D. Nelson, N. Ramkumar, B.K. Gale, Flexible, transparent, sub-100 μm microfluidic channels with fused deposition modeling 3D-printed thermoplastic polyurethane, J. Micromech. Microeng. 29 (2019), https://doi.org/10.1088/1361-6439/ab2f26.
[9] N. Vidakis, M. Petousis, N. Vaxevanidis, J. Kechagias, Surface roughness investigation of poly-jet 3D printing, Mathematics 8 (2020), https://doi.org/10.3390/math8101758.
[10] N. Bhattacharjee, A. Urrios, S. Kang, A. Folch, The upcoming 3D-printing revolution in microfluidics, Lab Chip 16 (2016), https://doi.org/10.1039/c6lc00163g.
[11] P. Juskova, A. Ollitrault, M. Serra, J.L. Viovy, L. Malaquin, Resolution improvement of 3D stereo-lithography through the direct laser trajectory programming: application to microfluidic deterministic lateral displacement device, Anal. Chim. Acta 1000 (2018), https://doi.org/10.1016/j.aca.2017.11.062.
[12] F. Zhu, J. Skommer, T. Friedrich, J. Kaslin, D. Wlodkowic, 3D printed polymers toxicity profiling: a caution for biodevice applications, Micro+Nano Mater., Devices, Syst. (2015), https://doi.org/10.1117/12.2202392.
[13] Q. Ge, Z. Li, Z. Wang, K. Kowsari, W. Zhang, X. He, J. Zhou, N.X. Fang, Projection micro stereolithography based 3D printing and its applications, Int. J. Extrem. Manuf. 2 (2020), https://doi.org/10.1088/2631-7990/ab8d9a.
[14] H.N. Chan, Y. Chen, Y. Shu, Y. Chen, Q. Tian, H. Wu, Direct, one-step molding of 3D-printed structures for convenient fabrication of truly 3D PDMS microfluidic chips, Microfluid Nanofluidics 19 (2015), https://doi.org/10.1007/s10404-014-1542-4.
[15] G. Gonzalez, A. Chiappone, K. Dietliker, C.F. Pirri, I. Roppolo, Fabrication and functionalization of 3D printed polydimethylsiloxane-based microfluidic devices obtained through digital light processing, Adv. Mater. Technol. 5 (2020), https://doi.org/10.1002/admt.202000374.
[16] N. Bhattacharjee, C. Parra-Cabrera, Y.T. Kim, A.P. Kuo, A. Folch, Desktop-stereolithography 3D-printing of a poly(dimethylsiloxane)-based material with sylgard-184 properties, Adv. Mater. 30 (2018), https://doi.org/10.1002/adma.201800001.
[17] K. Zhou, M. Dey, B. Ayan, Z. Zhang, V. Ozbolat, M.H. Kim, V. Khristov, I. T. Ozbolat, Fabrication of PDMS microfluidic devices using nanoclay-reinforced Pluronic F-127 as a sacrificial ink, Biomed. Mater. (Bristol) 16 (2021), https://doi.org/10.1088/1748-605X/abe55e.
[18] M. Wehner, R.L. Truby, D.J. Fitzgerald, B. Mosadegh, G.M. Whitesides, J.A. Lewis, R.J. Wood, An integrated design and fabrication strategy for entirely soft, autonomous robots, Nature 536 (2016), https://doi.org/10.1038/nature19100.

[19] V. Ozbolat, M. Dey, B. Ayan, A. Povilianskas, M.C. Demirel, I.T. Ozbolat, 3D printing of PDMS improves its mechanical and cell adhesion properties, ACS Biomater. Sci. Eng. 4 (2018), https://doi.org/10.1021/acsbiomaterials.7b00646.
[20] M.M. Durban, J.M. Lenhardt, A.S. Wu, W. Small, T.M. Bryson, L. Perez-Perez, D. T. Nguyen, S. Gammon, J.E. Smay, E.B. Duoss, J.P. Lewicki, T.S. Wilson, Custom 3D printable silicones with tunable stiffness, Macromol. Rapid Commun. 39 (2018), https://doi.org/10.1002/marc.201700563.
[21] X. Zeng, Z. Meng, J. He, M. Mao, X. Li, P. Chen, J. Fan, D. Li, Embedded bioprinting for designer 3D tissue constructs with complex structural organization, Acta Biomater. 140 (2022), https://doi.org/10.1016/j.actbio.2021.11.048.
[22] D.N. Heo, M.A. Alioglu, Y. Wu, V. Ozbolat, B. Ayan, M. Dey, Y. Kang, I.T. Ozbolat, 3D bioprinting of carbohydrazide-modified gelatin into microparticle-suspended oxidized alginate for the fabrication of complex-shaped tissue constructs, ACS Appl. Mater. Interfaces 12 (2020), https://doi.org/10.1021/acsami.0c05096.
[23] A. McCormack, C.B. Highley, N.R. Leslie, F.P.W. Melchels, 3D printing in suspension baths: keeping the promises of bioprinting afloat, Trends Biotechnol. 38 (2020), https://doi.org/10.1016/j.tibtech.2019.12.020.
[24] W. Wu, A. Deconinck, J.A. Lewis, Omnidirectional printing of 3D microvascular networks, Adv. Mater. 23 (2011), https://doi.org/10.1002/adma.201004625.
[25] T. Bhattacharjee, S.M. Zehnder, K.G. Rowe, S. Jain, R.M. Nixon, W.G. Sawyer, T. E. Angelini, Writing in the granular gel medium, Sci. Adv. 1 (2015), https://doi.org/10.1126/sciadv.1500655.
[26] T.J. Hinton, A. Hudson, K. Pusch, A. Lee, A.W. Feinberg, 3D printing PDMS elastomer in a hydrophilic support bath via freeform reversible embedding, ACS Biomater. Sci. Eng. 2 (2016), https://doi.org/10.1021/acsbiomaterials.6b00170.
[27] M.H. Kim, D. Banerjee, N. Celik, I.T. Ozbolat, Aspiration-assisted freeform bioprinting of mesenchymal stem cell spheroids within alginate microgels, Biofabrication 14 (2022), https://doi.org/10.1088/1758-5090/ac4dd8.
[28] M.E. Cooke, D.H. Rosenzweig, The rheology of direct and suspended extrusion bioprinting, APL Bioeng. 5 (2021), https://doi.org/10.1063/5.0031475.
[29] M. Zhu, Y. Wang, G. Ferracci, J. Zheng, N.J. Cho, B.H. Lee, Gelatin methacryloyl and its hydrogels with an exceptional degree of controllability and batch-to-batch consistency, Sci. Rep. 9 (2019), https://doi.org/10.1038/s41598-019-42186-x.
[30] N.J. Palpant, L. Pabon, C.E. Friedman, M. Roberts, B. Hadland, R.J. Zaunbrecher, I. Bernstein, Y. Zheng, C.E. Murry, Generating high-purity cardiac and endothelial derivatives from patterned mesoderm using human pluripotent stem cells, Nat. Protoc. 12 (2017), https://doi.org/10.1038/nprot.2016.153.
[31] A.K. Grosskopf, R.L. Truby, H. Kim, A. Perazzo, J.A. Lewis, H.A. Stone, Viscoplastic matrix materials for embedded 3D printing, ACS Appl. Mater. Interfaces 10 (2018), https://doi.org/10.1021/acsami.7b19818.
[32] A.M. Goldfain, P. Lemaillet, D.W. Allen, K.A. Briggman, J. Hwang, Polydimethylsiloxane tissue-mimicking phantoms with tunable optical properties, J. Biomed. Opt. 27 (2021), https://doi.org/10.1117/1.jbo.27.7.074706.
[33] R. Akhtar, M.J. Sherratt, J.K. Cruickshank, B. Derby, Characterizing the elastic properties of tissues, Mater. Today 14 (2011), https://doi.org/10.1016/S1369-7021(11)70059-1.
[34] Q. Li, L. Ma, Z. Gao, J. Yin, P. Liu, H. Yang, L. Shen, H. Zhou, Regulable supporting baths for embedded printing of soft biomaterials with variable stiffness, ACS Appl. Mater. Interfaces 14 (2022) 41695–41711, https://doi.org/10.1021/acsami.2c09221.
[35] Q. Wu, K. Song, D. Zhang, B. Ren, M. Sole-Gras, Y. Huang, J. Yin, Embedded extrusion printing in yield-stress-fluid baths, Matter 5 (2022) 3775–3806, https://doi.org/10.1016/j.matt.2022.09.003.
[36] G.R. Sanderson, Applications of Xanthan gum, Br. Polym. J. 13 (1981), https://doi.org/10.1002/pi.4980130207.
[37] D. Kang, G. Ahn, D. Kim, H.W. Kang, S. Yun, W.S. Yun, J.H. Shim, S. Jin, Pre-set extrusion bioprinting for multiscale heterogeneous tissue structure fabrication, Biofabrication 10 (2018), https://doi.org/10.1088/1758-5090/aac70b.
[38] M.T. Arigo, G.H. McKinley, An experimental investigation of negative wakes behind spheres settling in a shear-thinning viscoelastic fluid, Rheol. Acta 37 (1998), https://doi.org/10.1007/s003970050118.
[39] A.M.V. Putz, T.I. Burghelea, I.A. Frigaard, D.M. Martinez, Settling of an isolated spherical particle in a yield stress shear thinning fluid, Phys. Fluids 20 (2008), https://doi.org/10.1063/1.2883937.
[40] E. Moreno, A. Larese, M. Cervera, Modelling of Bingham and Herschel-Bulkley flows with mixed P1/P1 finite elements stabilized with orthogonal subgrid scale, J. Nonnewton Fluid Mech. 228 (2016), https://doi.org/10.1016/j.jnnfm.2015.12.005.
[41] K. Raj M, S. Chakraborty, PDMS microfluidics: a mini review, J. Appl. Polym. Sci. 137 (2020), https://doi.org/10.1002/app.48958.
[42] M. Tanyeri, S. Tay, Viable cell culture in PDMS-based microfluidic devices, Methods Cell Biol. (2018), https://doi.org/10.1016/bs.mcb.2018.09.007.
[43] N. Korin, M. Kanapathipillai, B.D. Matthews, M. Crescente, A. Brill, T. Mammoto, K. Ghosh, S. Jurek, S.A. Bencherif, D. Bhatta, A.U. Coskun, C.L. Feldman, D. D. Wagner, D.E. Ingber, Shear-activated nanotherapeutics for drug targeting to obstructed blood vessels, Science 337 (2012) (1979), https://doi.org/10.1126/science.1217815.
[44] H. Mollica, R. Palomba, R. Primavera, P. Decuzzi, Two-channel compartmentalized microfluidic chip for real-time monitoring of the metastatic cascade, ACS Biomater. Sci. Eng. 5 (2019), https://doi.org/10.1021/acsbiomaterials.9b00697.
[45] A.M.O. Pollet, E.F.A. Homburg, R. Cardinaels, J.M.J. den Toonder, 3D sugar printing of networks mimicking the vasculature, Micro (Basel) 11 (2020), https://doi.org/10.3390/mi11010043.
[46] M.A. Skylar-Scott, S.G.M. Uzel, L.L. Nam, J.H. Ahrens, R.L. Truby, S. Damaraju, J. A. Lewis, Biomanufacturing of organ-specific tissues with high cellular density and embedded vascular channels, Sci. Adv. 5 (2019), https://doi.org/10.1126/sciadv.aaw2459.
[47] A. Lee, A.R. Hudson, D.J. Shiwarski, J.W. Tashman, T.J. Hinton, S. Yerneni, J. M. Bliley, P.G. Campbell, A.W. Feinberg, 3D bioprinting of collagen to rebuild components of the human heart, Science (1979) 365 (2019), https://doi.org/10.1126/science.aav9051.
[48] B. Ayan, D.N. Heo, Z. Zhang, M. Dey, A. Povilianskas, C. Drapaca, I.T. Ozbolat, Aspiration-assisted bioprinting for precise positioning of biologics, Sci. Adv. 6 (2020), https://doi.org/10.1126/sciadv.aaw5111.
[49] N.P. Macdonald, J.M. Cabot, P. Smejkal, R.M. Guijt, B. Paull, M.C. Breadmore, Comparing microfluidic performance of three-dimensional (3D) printing platforms, Anal. Chem. 89 (2017), https://doi.org/10.1021/acs.analchem.7b00136.
[50] K. Ioannidis, R.I. Danalatos, S. Champeris Tsaniras, K. Kaplani, G. Lokka, A. Kanellou, D.J. Papachristou, G. Bokias, Z. Lygerou, S. Taraviras, A custom ultra-low-cost 3D bioprinter supports cell growth and differentiation, Front Bioeng. Biotechnol. 8 (2020), https://doi.org/10.3389/fbioe.2020.580889.